Electrical Resistivity Imaging of solute transport under transient conditions within a model hillslope transect.

Antonio Alves Meira Neto[1,2]*, Minseok Kim[3], Alejandro Cueva[3], Till Volkmann[3] and Peter A. Troch[1,3]

[1]University of Arizona, Department of Hydrology and Atmospheric Sciences

[2] Institute of Climate Studies, Federal University of Espírito Santo, Vitória, ES, Brazil

[3] University of Arizona, Biosphere 2

*Corresponding author: antoniomeira@gmail.com

Key points

1. This study proposes a simple method for the study of solute movement using ERI under transient conditions.

2. We applied a saline tracer onto a sloping soil lysimeter designed to reproduce the hydrologic behavior observed at the hillslope scale.

3. Our analysis provided observational insight into the role of water table dynamics in solute export at natural hillslopes.

ABSTRACT

The direct observation of water movement via Electrical Resistivity Imaging (ERI) can leverage the understanding of the processes that lead to the occurrence of variable residence times (RT) within the Critical Zone (CZ). While hydrological processes at natural landscapes are often space and time-variable, quantitatively estimating solute transport with ERI under transient conditions is challenging due to necessary considerations of moisture states and electrical properties of the medium. Here, we introduce the use of Periodic Steady State (PSS) theory applied to electrical resistivity of soils to provide a simple solution to the problems and report a laboratory experiment to test the proposed method. We used a 1 m^3 sloping lysimeter to represent the hydrological functioning of natural hillslopes, equipped with electrodes to provide cross-borehole images of bulk soil electrical conductivity and performed a 28-days experiment in which a periodic irrigation was applied. A saline tracer was added to the lysimeter in two irrigation pulses and subsequent pulses were applied until the tracer was flushed out. ERI-surveys and estimates of background soil-water conductivity were used to quantitatively estimate solute breakthrough throughout the different cross-sections. Integrated lysimeter-scale images were superimposed with the water table progression throughout the experiment to leverage the understanding of flow and transport processes responsible for the tracer mobilization. Our study introduces a novel method for laboratory experimentation at mesocosm scales using ERI and provides valuable insight into the role of water table dynamics in mediating the occurrence of variable flow pathways within hillslopes.

1. INTRODUCTION

The critical zone (CZ) is the region that extends from the bottom of the bedrock aquifer to the top of the plant canopies and it is where most the hydro-biogeochemical fluxes relevant to sustaining life on the planet take place (Chorover et al., 2007). The knowledge of transport-related phenomena at the subsurface is of great relevance for the understanding of CZ structure and functioning (Brooks et al., 2015), since it can inform the extent to which fresh water interacts with mineral surfaces, influencing the overall equilibrium of weathering reactions (Maher, 2010, 2011) and release of nutrients (Brantley et al., 2007). The spatial variability of weathering rates and mineralogy seen in natural landscapes can be explained in part by variable water fluxes and residence times imposed by topographic gradients (Lybrand and Rasmussen 2014, 2018; Zapata-Rios et al., 2015; Vazquez-Ortega et al., 2016) and heterogeneous soil properties. This natural variability is often accounted for by studying such interactions processes at the hillslope scale (Dontsova et al., 2009; Heimsath et al., 2013; Pohlman et al., 2016).

Most attempts to characterize residence times of water are based on the analysis of the aggregated catchment response (see review by McGuire and McDonnell, 2006), in which time-series of concentrations of one or multiple tracers are used in conjunction with rainfall and discharge values to infer transport properties of catchments. While such methods are useful, they can only provide a lumped representation of transport within hydrologic systems, and therefore lack local-scale process description. The study of local-scale flow and transport processes cannot only provide a physical interpretation of water transit times (Pangle et al., 2017), but is also a necessary step towards the improvement of watershed models, which commonly lack combined flow and transport processes description (McDonnell and Beven, 2014). In this way, the tracking and quantification of tracer movement allows for the direct observation of velocities and residence times of water within the subsurface, providing a great opportunity for understanding the internal functioning of the CZ.

In the last 25 years, electrical resistivity imaging (ERI) has been widely used as a non-invasive tool for investigating solute transport in the subsurface (Binley et al., 1996; Kemna et al., 2002; Singha and Gorelick, 2006; Koestel et al., 2008; Wehrer and Slater, 2015). ERI-methods are subject, however, to uncertainties arising from the ill-posedness and non-uniqueness of the

inversion process (Binley et al., 2015). Moreover, the soil bulk electrical conductivity (σ_b) estimated through ERI surveys is controlled by multiple variables. In order to convert the estimates of σ_b into fluid conductivity (σ_f), estimates of soil porosity (ϕ), water saturation (S), and eventually soil-surface conductivity (σ_s) are needed. This poses additional challenges to the quantitative assessment of solute transport through ERI methods.

Numerous strategies have been employed in order to circumvent the latter issue. One way forward is utilizing the parameters for petrophysical functions relating σ_b and its controlling variables (Friedman, 2005; Samouelian et al., 2005). However, information on such parameters for different kinds of soils are rarely available, adding the necessity of laboratory experiments (Rhodes, 1981; Grunat et al., 2013). Even in the case of laboratory-retrieved petrophysical parameters, the application of sample-based relationships to an ERI image will not necessarily be successful (Wehrer and Slater, 2015), since it will not account for the heterogeneity found in soils. Another alternative consists of imposing or assuming steady state (SS) conditions at either saturated or unsaturated conditions (Binley et al., 1996; Slater, 2002; Alumbaugh et al., 2004; Koestel et al., 2008), which is commonly performed in controlled experiments. Its main disadvantage comes from the limited range of processes that can be reproduced, as the majority of hydrological processes occurring in natural landscapes do not take place at steady-state conditions.

Nonetheless, a simple approach that takes advantage of repeatability of an experiment can be developed that allows for a quantitative characterization of solute transport under unsteady state conditions with spatially varying degrees of saturation. When a given system is forced following a repetitive regime of inputs, its internal states and outputs will eventually repeat themselves, and the system will enter a periodic steady state regime (PSS). This is akin to the notion of driven harmonic oscillation, which occurs, for example, when a force is repeatedly applied to a pendulum. The concept of PSS has been applied as a condition for the application of the Periodic Tracer Hierarchy (PeRTH, Harman and Kim, 2014; Kim et al., 2016) method. The PERTH method was envisioned for the extraction of transit time distributions when different tracers are applied to a system and relies on the observation of tracer concentrations at the system's outlet for its successful application (Wang et al., 2019).

Here, we present a time-lapse ERI-based study of unsteady state solute imaging at the sub-meter-scale using the PSS theory. Our experimental set-up utilizes a sloping 1 m^3 soil lysimeter that aims

at reproducing the hydrologic processes observed in natural hillslopes. We imposed a PSS by means of a repetitive irrigation schedule with the addition of a high-concentration saline tracer. The objectives of this paper are twofold: *First,* we propose a straightforward method for the estimation of tracer movement using ERI in that it does not require the fitting of parameters from petrophysical relationships and can be used to understand solute transport at transient conditions. *Second*, we use the retrieved images of the tracer movement throughout the irrigation experiment to characterize the (internal) flow and transport processes ultimately leading to the observed (external) tracer breakthrough.

2. SOLUTE TRACKING UNDER PERIODIC STEADY STATE

2.1. PROCEDURE FOR SOILS WITH NEGLIGIBLE SURFACE CONDUCTIVITY

For non-conductive soils, the soil bulk electrical conductivity ($\sigma_b, in\ \mu S/cm$) can be explained as a function of the conductivity of the soil water (σ_f), porosity (ϕ) and water-saturation (S), and is described by Archie's law (Archie, 1942) as:

$$\sigma_b = \sigma_f \phi^m S^n \tag{1}$$

where m is the cementation exponent, and n is the saturation exponent. In order to obtain values of σ_f from σ_b , the remaining variables and exponents need to be estimated. Under SS, the term $\phi^m S^n$ remains constant throughout the course of the injection, and the tracer migration can be analyzed by the ratio (σ_{rat}) between post-injection data-frames ($\sigma_{b_{post}}$) at an arbitrary time t, and the background conductivity image, $\sigma_{b_{pre}}$:

$$\sigma_{rat}(t) = \frac{\sigma_{b_{post}}(t)}{\sigma_{b_{pre}}(t)} = \frac{\sigma_{f_{post}}(t)\phi^m S^n}{\sigma_{f_{pre}}\phi^m S^n} \tag{2}$$

where $\sigma_{f_{post}}$ is the post-injection fluid conductivity and $\sigma_{f_{pre}}$ is the pre-injection fluid conductivity. The evolution of the conductivity ratio through time can be seen as a breakthrough curve of relative concentration under the assumptions of (1) full saturation (S = 1), (2) changes in σ_b occur only due to changes in σ_f, and (3) σ_f is a linear function of salt concentration (Binley et al., 1996). Examples of this approach include the pixel-based breakthrough curves estimated by Binley et al., (1996), or the voxel-based breakthrough curves estimated by Slater et al., (2000). Assuming that pre-injection

values of fluid conductivity can be estimated, equation **2** provides a solution of $\sigma_{b,post}$. Slater et al., (2002) used water samples collected from wells to both estimate the pre-injection σ_f and validate ERI-based breakthrough curves, finding good agreement for both magnitude and timing of tracer peaks. Koestel et al., (2008) successfully estimated the tracer breakthrough within an undisturbed soil monolith at unsaturated steady-state conditions by a similar approach. They assumed uniform distribution of σ_f prior to tracer injection and validated the internal breakthrough results by comparing ERI-estimates of σ_f with observations based on time domain reflectometry (TDR). For unsteady state conditions, the above-mentioned simplifications cannot be made since the factor S^n will vary over time and space. In this case, knowledge of the exponents in equation 1 is needed. Wehrer and Slater (2015) characterized the tracer breakthrough of the seepage water of a laboratory lysimeter under transient unsaturated conditions by comparison of shape measures (Koestel et al., 2011) of the breakthrough curves. In their study, they obtained values of σ_f by applying laboratory derived petrophysical functions (Grunat et al., 2013) onto the ERI-retrieved values of σ_b.

We define a PSS-cycle as the period where hydrologic states and fluxes are repeated (Harman and Kim, 2014). This can be achieved for example by repeating an irrigation sequence separated by equal time intervals. Under PSS, the variables in **1** become a function of the time relative to the beginning of a cycle (t^*):

$$\sigma_b(t^*) = \sigma_f(t^*)\phi^m S(t^*)^n. \quad (3)$$

The internal states and outputs achieved within a PSS-cycle will result from an interplay between internal properties (porosity, hydraulic conductivity and retention characteristics) and the input sequence: if, for example, the system under study is a soil lysimeter subject to an irrigation schedule, moisture states and fluxes can vary from saturated to unsaturated conditions both in space and time depending on the intensity and duration of the imposed irrigation sequence.

The experiment begins by first forcing the system to reach PSS by periodically adding water with background tracer concentrations and conductivity. We call this period "warmup" (w), which leads to the response of a warmup cycle as:

$$\sigma_b(t_w^*) = \sigma_f(t_w^*)\phi^m S(t_w^*)^n, \quad (4)$$

where t_w^* is the time relative to the beginning of the warmup cycle. After PSS reached, the progress σ_b within a cycle will be repeated at every cycle. The estimation of a representative warmup cycle can therefore be taken from any cycle within PSS conditions, or an average of all warmup cycles to account for between cycle variability that can potentially arise due to failure in repeating the exact input sequence. After that, an "injection" cycle is performed, in which water with contrasting concentrations (and conductivity) is applied. Subsequent cycles are then imposed with background concentrations until tracer recovery is satisfactorily achieved. The cycles from injection until the end of recovery are called active (A), and the soil-bulk conductivity can be written as:

$$\sigma_b(t_k^*) = \sigma_f(t_k^*)\phi^m S(t_k^*)^n \tag{5}$$

where t_k^* is the time relative to the beginning of the k^{th} active-cycle. By dividing each active-cycle response by the warmup-cycle response, the following expression can be written for any active cycle:

$$\frac{\sigma_b(t_k^*)}{\sigma_b(t_w^*)} = \frac{\sigma_f(t_k^*)}{\sigma_f(t_w^*)} \cdot \frac{\phi^m S(t_k^*)^n}{\phi^m S(t_w^*)^n}, \tag{6}$$

Since the term $\phi^m S(t)^n$ is the same for warmup and active periods, we arrive at the estimation of σ_{rat} for the unsteady state case as:

$$\sigma_{rat}(t_k^*) = \frac{\sigma_b(t_k^*)}{\sigma_b(t_w^*)} = \frac{\sigma_f(t_k^*)}{\sigma_f(t_w^*)}. \tag{7}$$

Similarly to the steady state case, assuming the pore-water conductivity prior to injection is estimated, equation **7** provides a solution for σ_f at any arbitrary time t.

2.2. PROCEDURE FOR SOILS WITH SURFACE CONDUCTIVITY

The bulk electrical conductivity of soils with significant surface conductivity follows a similar form as in equation 1, however with an additional term representing the solid surface intrinsic conductivity ($\sigma_S, in\ \mu S/cm$). Here we represent σ_b following the model of Waxman and Smith (1968) as:

$$\sigma_b = w\sigma_f\phi^m S^n + \sigma_S \tag{8}$$

where w is a fitting parameter. In this case, the ratio-based solution presented in **2.1** will not yield a solution for σ_f. To circumvent this issue, an additional warmup phase is required prior to the injection phase. The additional warmup phase will follow the same prescribed forcing but have different but known background tracer concentrations and conductivity. In this case, we re-write equation 6 as:

$$\sigma_{b_1}(t_w^*) = w\sigma_{f_1}(t_w^*)\,\phi^m S(t_w^*)^n + \sigma_S, \tag{9}$$

$$\sigma_{b_2}(t_w^*) = w\sigma_{f_2}(t_w^*)\,\phi^m S(t_w^*)^n + \sigma_S, \tag{10}$$

Where σ_{b_1} stands for the bulk conductivity during warmup with fluid conductivity σ_{f_1}, while σ_{b_2} stands for bulk conductivity during a second warmup period with fluid conductivity σ_{f_2}. The difference between equations 10 and 9 yield:

$$\sigma_{b_2}(t_w^*) - \sigma_{b_1}(t_w^*) = w\phi^m S(t_w^*)^n\left[\sigma_{f_2}(t_w^*) - \sigma_{f_1}(t_w^*)\right], \tag{11}$$

After rearranging the terms, we obtain an estimate of the product of unknown terms,ψ at any moment t^*:

$$\psi(t^*) = w\phi^m S(t_w^*)^n = \frac{\sigma_{b_2}(t_w^*) - \sigma_{b_1}(t_w^*)}{\sigma_{f_2}(t_w^*) - \sigma_{f_1}(t_w^*)}. \tag{12}$$

Once estimated, ψ can be used to solve for σ_f by subtracting each active-cycle response by a warmup-cycle response, allowing the following expression to be written for any active cycle:

$$\sigma_b(t_k^*) - \sigma_{b_X}(t_w^*) = w\phi^m S(t_w^*)^n\left[\sigma_f(t_k^*) - \sigma_{f_X}(t_w^*)\right], \tag{13}$$

in which *X* represents either first (1) or second (2) warmup background concentrations. By substituting 12 into 13 and rearranging accordingly one obtains:

$$\sigma_f(t_k^*) - \sigma_{f_X}(t_w^*) = \frac{\sigma_b(t_k^*) - \sigma_{b_X}(t_w^*)}{\psi(t^*)}, \tag{14}$$

As in the case of soils with negligible surface conductivity (equation 7), assuming known background pore-water conductivity of warmup periods 1 and 2 is, equation **14** provides a solution for σ_f at any arbitrary time t.

206 ## 3. MATERIALS AND METHODS

207 ### 3.1. The miniLEO lysimeter

208 The miniLEO (**Figure1-A**) is a 10-degree sloping soil lysimeter with 1m^3 capacity (0.5 m x 2.0 m
209 x 1.0 m) located at the Biosphere 2 facility in Oracle, Arizona. The lysimeter is a small-scale
210 replicate of the Landscape Evolution Observatory (LEO) artificial hillslopes (Pangle et al., 2015)
211 constructed at the same facility. The interior walls and floor of the lysimeter are coated with a non-
212 conductive abrasion-resistant waterproofing system (DuralDeck, Euclid Chemical Company). The
213 miniLEO rests on 4 load cells (Honeywell Model 41 Load Cell) and is equipped with a sprinkler-
214 based irrigation system composed by multiple sprinkler heads (not shown) that can be adjusted to
215 deliver rain intensities ranging from 10 to 30 mm/h. For this experiment the irrigation system was
216 adjusted for a single rain intensity (14mm/h, using 3 sprinkler heads) and multiple trial runs were
217 performed to achieve a homogenous rainfall distribution over the soil surface. The lower-right end
218 wall of the lysimeter act as a seepage face (at atmospheric pressure, no suction is applied at this
219 boundary condition), and is composed of a perforated plastic sheet separated from the basaltic soil
220 by a 10 cm basalt gravel layer. Seepage water is collected at a gutter and is routed to a tipping
221 bucket (ONSET HOBO model RG3), allowing for the computation of the volumetric discharge
222 out of the system. Discharge samples were collected at each hour throughout the course of the
223 experiment. Vertically arranged Prenart® suction lysimeters at 5 different depths (5, 20, 35, 50
224 and 85 cm) are located along 3 sampling verticals (at 0.65, 1.25 and 1.85 m from the left wall,
225 Erro! Fonte de referência não encontrada.**-A**). Suction lysimeters are routed to an airtight acrylic
226 box (not shown) containing reusable plastic veils for sample collection at each corresponding
227 location. The acrylic box is connected to a vacuum pump adjusted for -0.5 Bar suction, allowing
228 for simultaneous sample collection from all locations. Two sensors were co-located with the
229 suction lysimeters (with an approximately separation of 5 cm in the x-direction): Decagon® MPS-
230 2 matric potential sensors, in this study were used to provide temperature readings and Decagon®
231 5TM for measurements of volumetric soil water content. Additionally, two Campbell CS451
232 pressure transducers were installed at the lysimeter floor (triangles in **Figure 1-A**).

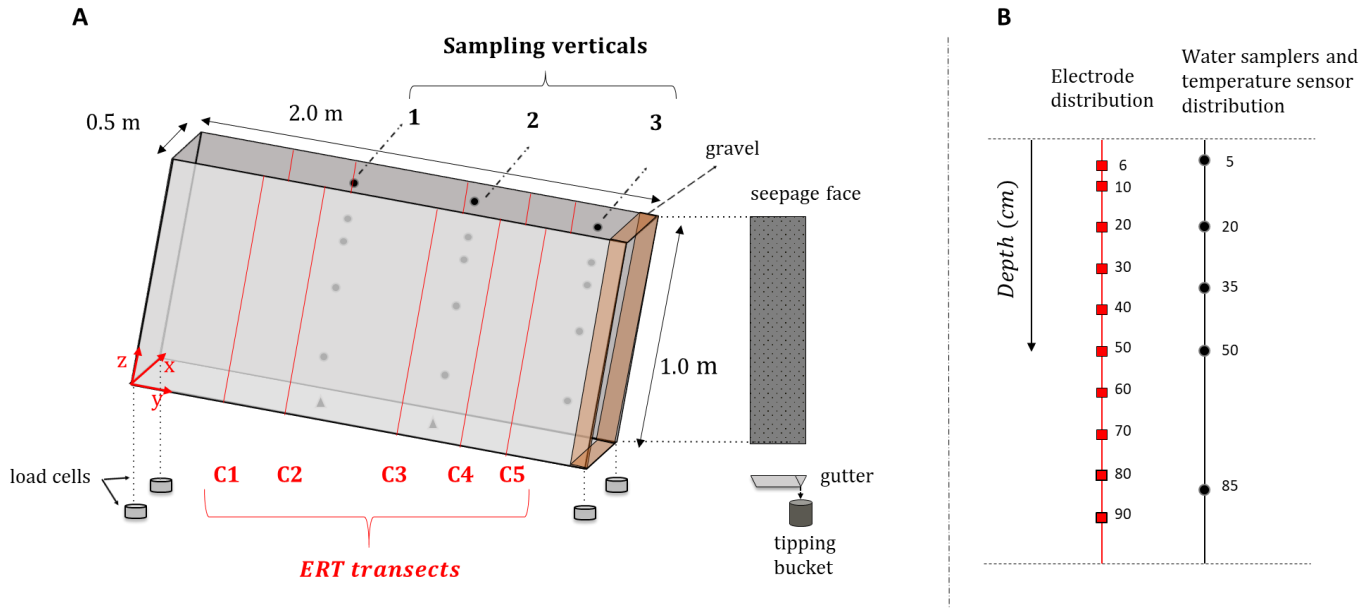

233

234

Figure 1 Schematic view the miniLEO soil lysimeter. A- Overview of the lysimeters dimensions, sampler locations, ERT verticals (C1 through C5) along the walls and overall instrumentation. Triangles represent Campbell CS451 pressure transducers. The Coordinate system (x,y and z directions) used throughout the text is highlighted in the lower end of the lysimeter. The location of the vertical gravel layer is shown in brown. Aside from this layer, the lysimeters volume was filled with the basaltic loamy sand. A metallic structure (not shown here) responsible for supporting the lysimeters weight and keeping it at a 10° angle did not allow for a uniform distribution of ERT verticals along the y-axis. B- Depth distribution of stainless-steel electrodes (red) and water samplers (Prenart ® suction lysimeters – black circles).

235

236 The material within the miniLEO is a basalt tephra extracted from a deposit in northern Arizona
237 that was further ground on site to a loamy sand texture. The final texture distribution was achieved
238 by sieving and remixing different size fractions of the original basalt so that a larger percentage of
239 fines could be achieved (Dontsova et al., 2009). This procedure led to a final texture consisting of
240 approximately 85% sand-size particles (≥ 50 and < 2000 µm), 12% silt-size particles (≥ 2 and <
241 50 µm), and 3% clay-size particles (< 2 µm). The material, herein referred to as basaltic soil, is the
242 same as in the LEO hillslopes and was chosen as part of the investigation of the coevolution of
243 soils and landscape complexity mediated by physical and biogeochemical processes (Pangle et al.,
244 2015). The intended low content of fine particles (approx. 32 g kg-1) should allow for an easier
245 detection of incipient secondary mineral formation (Pohlman et al., 2016). Even though clay-sized
246 particles are present in the basaltic soil, no secondary minerals were estimated as part of the
247 basalt's mineralogical composition (Dontsova et al., 2009; Pangle et al., 2015; Pohlman et al.,

2016). In addition to that, we assumed that no considerable clay formation took place through the course of the experiment, and a treatment of the soil according to the procedure for soils with negligible surface conductivity was followed (item **3.2**).

The basaltic soil was added to the lysimeter in December 2016, through a procedure consisting of sequentially adding 32 cm increments of loose soil, which were then compacted to 25cm. During this procedure, the first 10 centimeter from the seepage face were occupied by the original gravel-size basaltic tephra to serve as a drainage layer.

10 ERI verticals (located at y = 0.25, 0.55, 1.1 1.4, and 1.63) containing 10 electrodes each are distributed along both walls of the lysimeter, as seen in **Figure1-A** and **B**. The location of the ERI-verticals was chosen in order to avoid overlap with sensor-verticals and also due to inaccessibility of certain portions of the lysimeter wall that were blocked by the metal structure responsible to keep the lysimeter at its 10 degree slope. This layout allows for acquisition of 5 cross-sectional resistivity images along different distances, hereafter referred as C1 through C5, in which the number 1 represents the upper most cross section (y = 0.25 m) and 5 the lower most (y = 1.63 m). The electrode distribution of each vertical follows a 10 cm interval spacing, with the exception of the first electrode position (**Figure1-B)**. The electrodes consist of 3 mm diameter stainless steel rods secured through plastic cable glands installed through orifices at the lysimeter walls. The electrodes were installed prior to the soil packing and the orifices were sealed with the same non-conductive water-proofing system used internally.

3.2. Periodic steady state (PSS) experiment

The PSS experiment described here served originally as an application of the Periodic Tracer Hierarchy (PERTH) method (Harman and Kim, 2014), designed to observe time-varying transit time distributions. While not intended to be an experiment for quantification of tracer movement, it conformed to all pre-requisites and experimental needs to test the proposed ERI-PSS method. The experiment was conducted between June 22nd and July 21st 2018 and consisted of 15 cycles (48 hours per cycle) in which a day with 2 consecutive rainfall pulses was followed by a dry day. **Figure 2-A** depicts the progression of the PSS cycles: During days with rain, two 3-hour-long pulses at a target intensity of 14 mm/hr were separated by 2 hours, and applied from 8:30 to 11:30 and from 13:30 to 16:30, while during dry days there was no rainfall application. **Figure 2-B** highlights the three distinct moments of the experiment: Initially, a warm-up period, necessary for

the system to reach a periodic steady state was imposed (the choice of 3 warm-up cycles is simply illustrative: the actual progression is shown in Figure 3). The warm-up irrigation water was kept at a background EC of 40 uS/cm (gray). Once PSS was achieved, irrigation water containing LiCl at 0.35g/l for a target conductivity of 1000 uS/cm was used with the rain system and applied to the lysimeter throughout a whole cycle (two rain-pulses, in green). Following the injection cycle, additional recovery cycles at background concentration were followed until water samples at the sampling locations reached pre-injection conductivity values. Soil-water samples from the suction lysimeters were collected at 9:00, 14:00 and 19:00 every day. The choice of this sampling scheme was related to availability of personal on site.

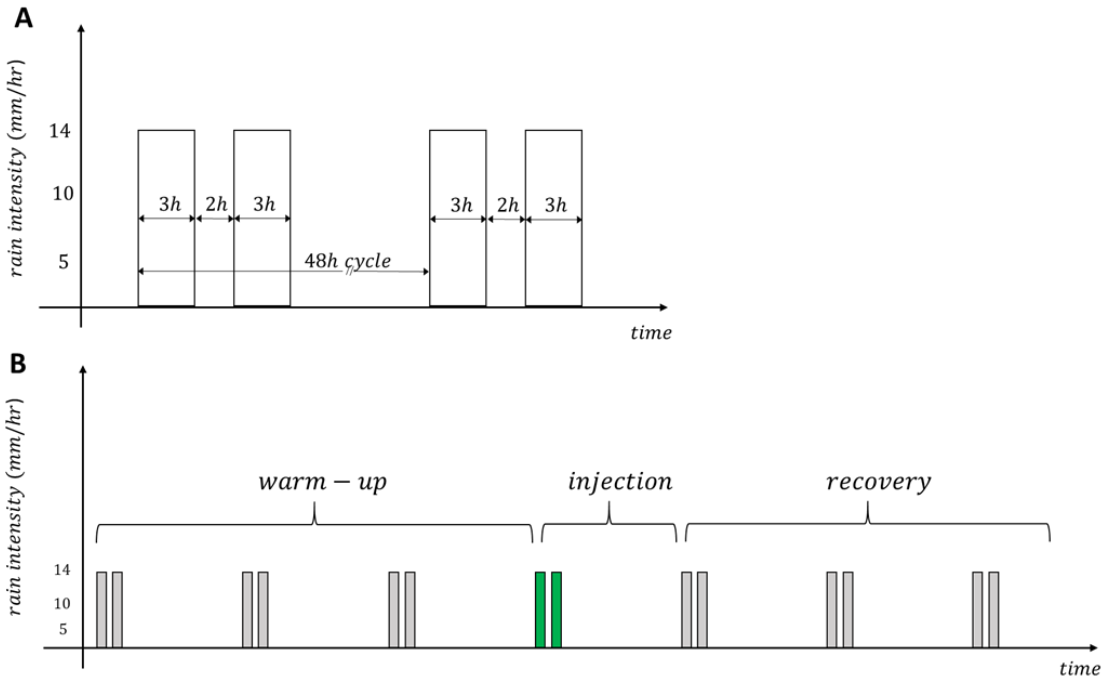

Figure 2 Schematic of the 48 hours cycle of rain application imposed at the miniLEO lysimeter at target rainfall intensity rate. B – Schematic of the progression of the experiment, highlighting the existence of 3 distinct groups of cycles: warm-up, injection and recovery. Green color represents the contrasting concentration of the rain pulses of injection in comparison with background concentration of the other cycles (gray). Figures are not to scale and serve the purpose explaining the overall progression of the experiment. Here, the number of warm-up and recovery cycles are also illustrative.

3.3. ERT measurements and data analysis

3.3.1. Data acquisition and pre-processing

Measurements of soil resistance (R −ratio of measured voltage between a pair of electrodes by the current injected between another pair or electrodes) were performed using the 8 channel Supersting R8 (Advanced Geosciences Inc.) resistivity meter. We followed a time-lapse cross-borehole survey designed to obtain 2D cross-sectional images at the 5 distances along the lysimeter. 2D cross-borehole configurations allow for quick image acquisition and have been widely used for studies of solute transport and plume migration in a variety of environments (Slater et al., 2000; Kemna et al., 2002; Looms et al., 2008; Perri et al., 2012; Bellmunt et al., 2016). A skip-dipole (Slater et al. 2000) measurement scheme with 2 and 3 electrode distances as the assigned skip, representing 248 measurements to be taken per cross-section (including reciprocals). A survey consisted of repeating the same scheme from cross-sections 1 through 5, resulting in a total of 1240 measurements per run. A total of 1190 surveys were performed between June 22nd 2018 and July 21st 2018, with each survey taking approximately 35 minutes. Poor soil-electrode contact during dry days allied to the low-conductivity water used in the rain pulses made it impossible for all readings to be taken at all surveys. This led to a reduction of the total measurements to an average of 1182 per survey (237 measurements per cross section, in average).

An error analysis procedure was conducted prior to the inversion. We first excluded obvious outliers by removing measurements with reciprocal error (ϵ_{recip}, Slater et al., 2001) greater than 5%, which resulted in a 7% reduction of the initial number of measurements. Following that, we estimated an error model for each survey in order to estimate weights to be used in the inversion (Slater et al. 2001, Koestel et al., 2008, Wehrer and Slater, 2015). This was done by binning the reciprocal measurements ($\overline{R}$) values in 10 classes with increasing order of magnitude and fitting a linear relationship between binned values of $\bar{R}$ and ϵ_{recip}, from which the slope and intercept were retained.

3.3.2. ERI Inversion and post-processing

The surveys were inverted with the code R3t (Binley, 2013), which estimates the spatial distribution of resistivities from measured potential and current values. We used the software Gmsh (Geuzaine and Remacle, 2009) to generate a three-dimensional finite element mesh consisting of 20640 tetrahedral elements with characteristic length of 5 cm. A time-lapse ERI

inversion scheme based on the difference regularization method of Labrecque and Yang (2001) was used in this study. This method allows for faster convergence and tends to minimize systematic errors. First, a reference data-set to be used as the a priori model for subsequent inversions is inverted according to the following objective function:

$$\Psi_d = (\mathrm{W_d}[\boldsymbol{d} - f(\boldsymbol{m})])^2 + \alpha(\mathrm{W_m}\boldsymbol{m})^2, \quad (15)$$

Where $\boldsymbol{d}$ is the vector of measured resistances ($\mathrm{O}hm$), $\boldsymbol{m}$ is the model vector of resistivities ($\mathrm{O}hm.m$), $f(\boldsymbol{m})$ is the forward solution of the resistances, $\mathrm{W_d}$ is a matrix containing the data weights, $\mathrm{W_m}$ is the roughness matrix, which is used to generate a smooth solution by penalizing differences between adjacent values of modelled resistivities and α is a smoothing parameter, which assigns a weight to the second term of the objective function. The first term of the objective represents the misfit between modelled and measured data, while the second is a measure of smoothness of the forward model. After the reference data-set is inverted, the data vector ($\boldsymbol{d}$) is modified for the subsequent data-sets as:

$$\boldsymbol{d} = \boldsymbol{d}' - \boldsymbol{d_{ref}} + f(\boldsymbol{m_{ref}}) \quad (16)$$

Where $\boldsymbol{d}'$ is the vector of measured resistances at a subsequent time, $\boldsymbol{d_{ref}}$ represents the measured resistances used in the reference data-set and $f(\boldsymbol{m_{ref}})$ is the forward solution of the reference data-set. A new objective function based on the minimization of the differences between current and reference data-sets and the smoothness term is then calculated:

$$\Psi_d = (\mathrm{W_d}[\boldsymbol{d} - f(\boldsymbol{m})])^2 + \alpha\left(\mathrm{W_m}\left[\boldsymbol{m} - \boldsymbol{m_{ref}}\right]\right)^2, \quad (17)$$

Two-dimensional cross-sectional resistivity images at the 5 transects were extracted from the inverted three-dimensional fields of resistivities and further converted to conductivity values ($\mu S/cm$). Since electrical conductivity is influenced by temperature (Campbell et al., 1948), the resulting conductivity values were corrected to a reference temperature by:

$$\sigma_b(T_{ref}) = \frac{\sigma_b(T)}{1 + 0.02(T - T_{ref})} \quad (18)$$

Where T is the in-situ temperature provided by the MPS2-2 matric potential sensors (see 3.1), and T_{ref} is a reference temperature (25 ^{o}C). Measurements from the co-located temperature sensors

were spatially interpolated and extrapolated to generate spatial temperature estimates at the cross-sections at the different times.

3.4. Chloride Breakthrough Analysis at PSS

3.4.1. Estimation of Cross-Sectional panels of σ_f

In order to obtain final estimates of conductivity values at each cross-section according to the methods outlined in section 2, the following procedure was followed: First, the soil water conductivity (σ_f) measurements taken at each sampling location during warm-up cycles were temporally averaged and a single warmup cycle response ($\bar{\sigma}_{f,W}$) at each location was created. Following that, values $\bar{\sigma}_{f,W}$ were spatially linearly interpolated at the locations of the cross-sections. Second, estimated cross-sectional bulk conductivities from the warmup period were averaged onto a single warmup cycle response ($\bar{\sigma}_{b,W}$). As previously mentioned, the basaltic soil can be considered not to have significant surface conductivity. Therefore, the injection and recovery cycles were corrected following equation 7 producing cross-sectional estimates of soil-water conductivity, $\bar{\sigma}_{f,A}$. We obtained the chloride concentrations from soil-water samples ($C_{Cl,Obs}$) using a linear relationship calibrated in the laboratory ($r^2 = 0.99$) relating chloride concentration ($\mu mol/L$) and electrical conductivity for the water ($\mu S/cm$) at 25°C as a reference temperature. Finally, ERI-based values of concentration ($C_{Cl,ERT}$) were obtained by converting $\bar{\sigma}_{f,A}$ into values of concentration using the relationship.

3.4.2. Estimation of depth-averaged profiles of σ_f and velocity of center of mass

We produced depth-averaged profiles of $C_{Cl,ERT}$ at 10-cm spacing for visual assessment of chloride breakthroughs. For evaluation of the results, values of $C_{Cl,Obs}$ from the 3 water sampling verticals were superimposed onto the ERI-cross sections by linear interpolation, while $C_{Cl,ERT}$ values were averaged at the equivalent locations. Cross-sections 1 and 2 were compared with vertical 1 to avoid extrapolation of water-sampler data beyond the measurement verticals during the active period. We quantified the progression of the tracer at each cross-section by first estimating the center of mass of each image and computing the time necessary for the latter to reach different depths.

3.4.3. 2-dimensional images of chloride concentration across the lysimeters length.

In order to allow for a better assessment of the chloride movement across the lysimeters length, 2-dimensional panels of chloride concentration from the moment of injection and onwards were created based on the spatial interpolation of depth averaged profiles across the domain of the lysimeter. Water table estimates obtained from the pressure transducers were linearly interpolated for the same region are also provided for this analysis.

3.4.4. Chloride Mass Balance comparisons for the whole lysimeter.

A comparison between observed and ERI-estimated chloride mass balances from the chloride injection and onwards were performed according to the following procedure. We first estimated the observed mass of chloride (M_{obs}) within the lysimeter was estimated according to the following equation:

$$M_{obs}(t) = I(t).C_{in} - O(t).C_{out}(t) \quad (19)$$

Where t represents the time stamp, I is the irrigation flux (l/min), C_{in} is the concentration of added chloride µmol/l, O is the discharge out of the lysimeters seepage face (l/min) and C_{out} is the chloride concentration at the discharge, in µmol/L. C_{in} is taken to be constant since the barrels with irrigation water were previously mixed with LiCl. The ERI-based estimates of chloride mass within the lysimeter (M_{ERT}) were estimated by multiplying the 2-dimensional panels of concentration described in the item 3.4.3 by 2-dimensional panels of water content taken as spatially interpolated fields from the original 5TM water content sensors.

4. RESULTS and DISCUSSION

4.1. Hydrologic assessment of the experiment

The overall progression of the experiment can be seen in **Figure 3**. Seven warmup irrigation cycles occurred prior to the injection cycle (8th cycle), followed by another 7 recovery cycles. **Figure 3A** shows the irrigation intensity applied through the several pulses as well as measured seepage-face discharge, whereas the load-cell mass changes are shown in **Figure 3B**. The estimated mean rainfall intensity was 13 mm/hr per pulse, with a standard deviation of 3 mm/hr (Coefficient of variance of 23%). Such variability occurred due to malfunctioning of the micro-controller that adjusts the pressure at the inlet of the tubbing system that distributes water to the sprinklers. The

resulting spatial distribution of irrigation intensities resulted in higher irrigation intensities closer to the seepage face was noted where the average intensity at the upper third was approximately 10 mm/hr, followed by 12 and 15 mm/hr at middle-slope and seepage face thirds respectively. Even though the system quickly reached a PSS, as seen in the variations in mass (**Figure 3B**), additional cycles were performed due to the issues mentioned previously. Electrical issues within the data-logging system during the cycles 1 and 3 led to poor estimation of mass and discharge values. **Figure 3C** shows the electrical conductivity of irrigation and discharge throughout the experiment. The irrigation water during warmup cycles was kept at an average of 41 $\mu S/cm$ with standard deviation of $\pm$ 2 $\mu S/cm$, while during injection a conductivity of 1040 $\mu S/cm$ was achieved (in black, **Figure 3C**). A delayed tracer response can also be identified where the discharge conductivity is seen to increase after the first cycle of the recovery period (Cycle 9, day 2 in Figure 3-C).

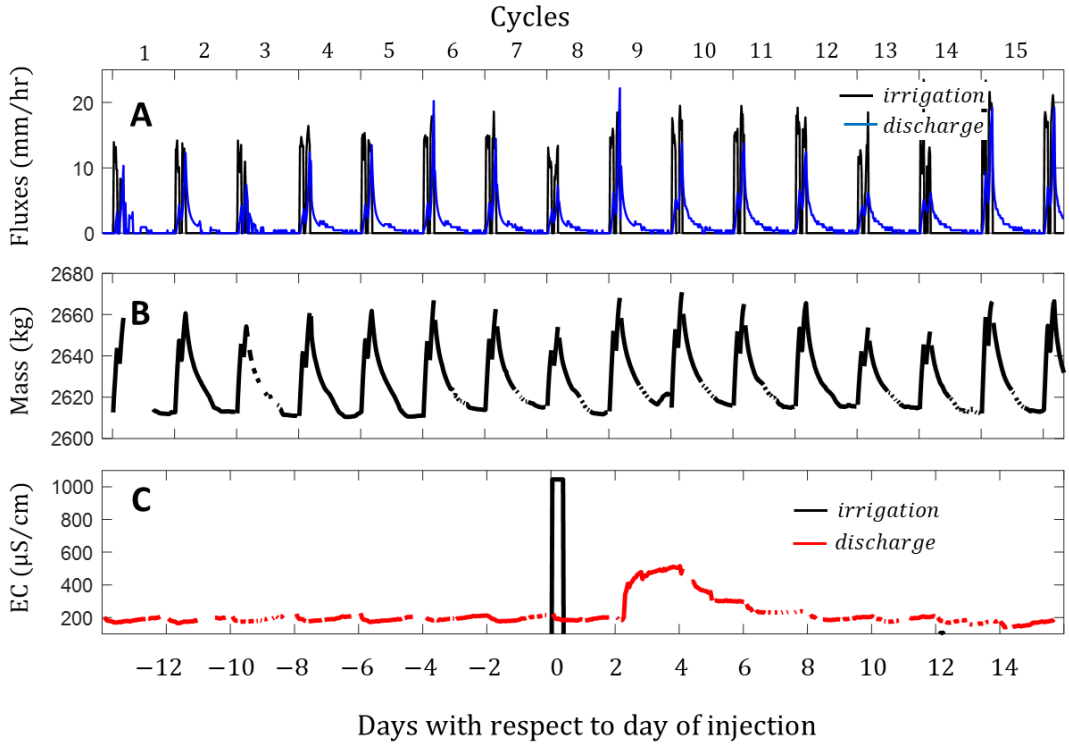

Figure 3 Hydrologic progress of the miniLEO lysimeter under a Periodic Steady State throughout the experiment. A- Irrigation (mm/hr) sequence applied throughout the experiment (black) and discharge (mm/hr) from the lysimeters seepage face (blue). B- Mass variations (kg) registered through the load cells indicate the increase in mass due to irrigation pulses and drainage periods. Equipment failure during the cycles 1 and 3 were responsible for missing values of mass which and poor estimates of discharge for those periods. C- Conductivities of irrigation (black) and discharge (red) fluxes.

Additional insights on the hydrologic processes within a cycle can be gained by analyzing both external and internal responses. **Figure 4A** shows the responses of the representative 48-hour cycle, shown as the average of all observed cycles for irrigation, discharge and storage. It is possible to see the double peaked response in storage and discharge resulting from the sequential irrigation pulses, followed by a recession period. Furthermore, we estimated the water tables responses by linearly interpolating the observed values from the pressure transducers (**Figure 1A**) for a better assessment of the degrees of saturation occurring within the lysimeter. **Figure 4B** shows the approximate water table location at the instants 3, 5, 8, 16 and 48h. While initially absent, the water table rises to a first peak at t = 3h, followed by a quick recession due to the absence of rainfall between t = 3h and t = 5h. With the end of the second irrigation pulse the water table reaches its second peak at t = 8h, which is followed by a recession (see t = 16h) and the absence of a water table characterizing the initial conditions of the cycle.

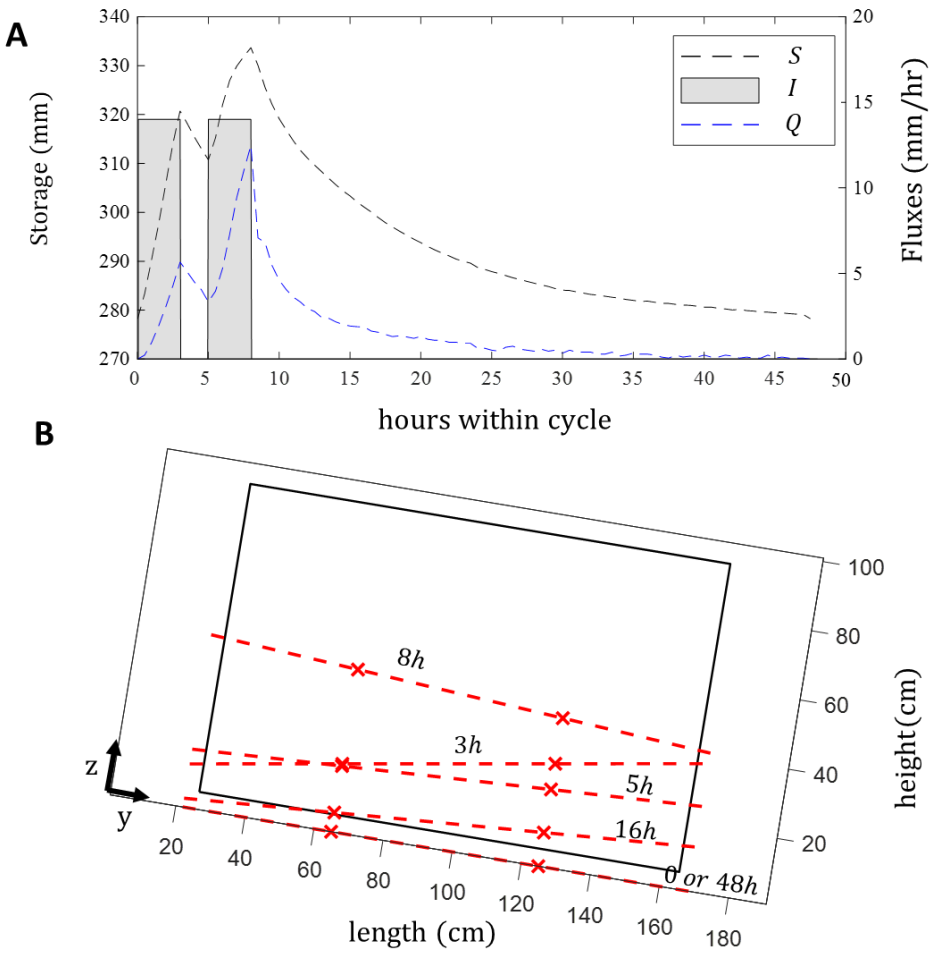

Figure 4 Characteristic (average) hydrologic responses within one cycle. A - Sequence of two 2-hour long irrigation pulses (gray bars) separated by a 2-hour period resulting increasing storage (black dashed line) and discharge (blue dashed line), followed by a recession period. B - Approximate location of the water table measured by pressure transducers (red x symbols), linearly interpolated throughout the ERI domain (inner square).

4.2. Warmup analysis

Figure 5-A shows the average warmup soil-water conductivity ($\overline{\sigma}_{f,W}$) per sampling location for the 3 sampling verticals over cycles 1 through 6. Horizontal bars depict the temporal variability (as one standard deviation) observed throughout the warmup cycles. A gradient of increasing

values $\boldsymbol{\sigma_f}$ with soil depth is suggested as a function of distance from the outlet. The pattern of $\boldsymbol{\sigma_f}$ can be attributed to the release of solutes from the basaltic material into solution occurring as the result of geochemical weathering. An analysis performed by Pohlman et al., (2016) on the hydro-geochemical behavior of the LEO hillslopes showed that the regions further from the outlet experience enhanced rates of weathering due to longer rock-water contact times and lower fluxes.

During the warmup period the ERI-acquisition-system faced 2 stoppages, making it impossible to fully observe the cycles 5, 6 and 7. For this reason, we used cycles 1 through 4 for estimation of the pre-injection bulk conductivity values $\boldsymbol{\sigma_{b,W}}$. For the purpose of visualization, **Figure 5-B** shows cross-sectional averages of bulk conductivity for those cycles. The repeatability achieved throughout the experiment can be seen as the spike in $\boldsymbol{\sigma_b}$ values due to the irrigation pulses (represented by the vertical lines), followed by a falling limb, associated with the decrease in soil moisture. It can also be seen that average values increase from the cross-section closest to the outlet (C5) to the cross-section located upslope (C1). This behavior can be attributed to a combination of average moisture contents per cross-section and the observed increase in values $\boldsymbol{\sigma_f}$ between the outlet and the upper boundary of the lysimeter, as seen in **Figure 5-A.**

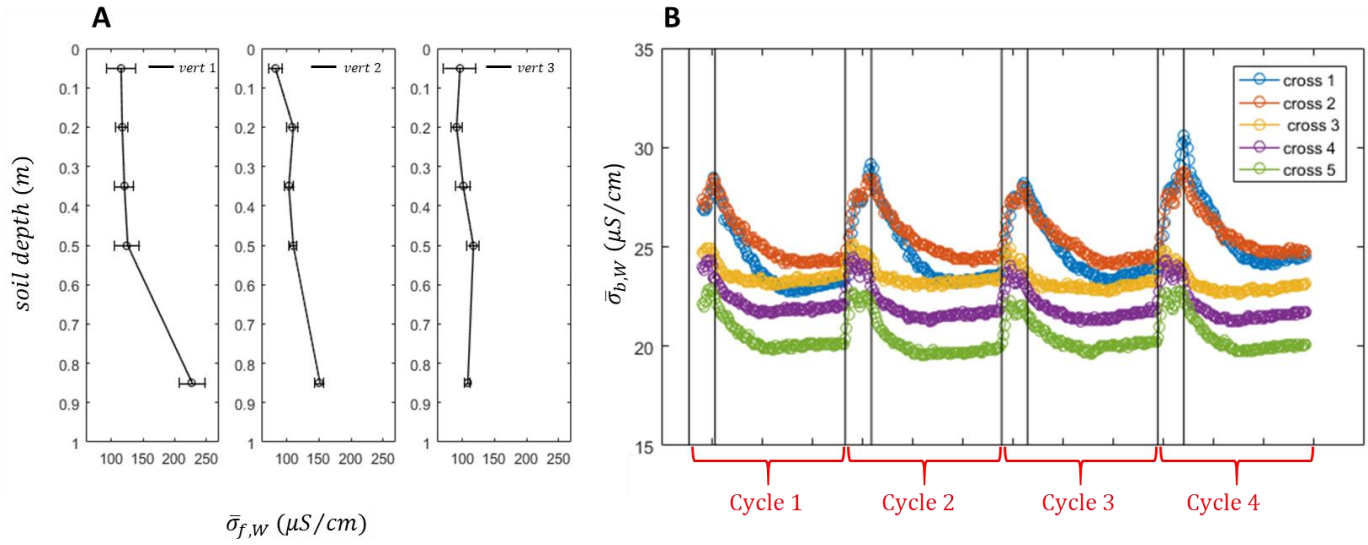

Figure 5 Patterns of bulk conductivity and fluid conductivity during warmup. A- Average σ_f obtained for the 3 water sampling verticals from the suction cups for the warmup period. Horizontal bars represent the standard deviation of all

measurements taken. The observed low variability in σ_f per sampling led to the choice of constant (average) values in solving for σ_f after injection. B-ERI measurements: cross-sectional averages of σ_b for cycles 1 through 4, used to estimate the pre-injection response. The σ_b trajectories over time illustrate the repeatability of the electrical conductivity as a response to a periodic oscillation of the internal variables. Vertical bars represent beginning and end of irrigation pulses for each cycle.

4.3. Injection analysis

Observed values of $\boldsymbol{\sigma_f}$ across all warmup cycles taken from the suction lysimeters were used to produce spatial estimates of background $\boldsymbol{\overline{\sigma}_{f,W}}$ for each cross-section (see Methods). We then normalized these cross-sectional estimates for each active cycle ($\boldsymbol{\sigma_{b,A}}$) by the respective average warmup cycle ($\boldsymbol{\sigma_{b,W}}$) and obtained estimates of $\boldsymbol{\sigma_{f,A}}$ by applying equation 7. After that we converted convert $\boldsymbol{\sigma_{f,A}}$ into values of concentration using a laboratory-derived relationship (see Methods 3.4).

The in-situ estimation of the spatial distribution of background conductivity ($\boldsymbol{\overline{\sigma}_{f,W}}$) throughout the warmup cycle is arguably a critical step for the application of our ERI-PSS procedure, as these values will be used to normalize bulk conductivities for injection subsequent recovery cycles, as seen in Equation 7 and 14. As seen in Figure 1, two ERI cross sections fall outside of the water sampler domain, which lead to the extrapolation of sampled values of conductivity to C1 and C2. We suggest that other applications of this method should attempt to obtain sampled values of soil conductivity for regions both within as well as outside of the survey domain. The issue of prior determination of background fluid conductivity has been a common pre-requisite for other laboratory based ERI applications of solute monitoring (Slater et al., 2002; Koestel et al., 2008; Wehrer and Slater, 2017).

While our sub-meter scale study might arguably be more adequate for laboratory settings, in which observations of background fluid conductivity are easier to obtain, some observations can be made about a possible field extension of the proposed method. *First*, the need for a warmup-period might be an asset for the determination of the background conductivities since a known conductivity to be previously used might help creating a more homogeneous $\boldsymbol{\sigma_f}$ field. *Second*, when previous background determination is not possible, the results reported as ratios between post-injection and

background can still be useful for understanding important transport processes taking place at plot scale.

Panels of retrieved values of concentration are shown in **Figure 6**, for 4 different days at 14:00, starting from the injection cycle. Differences in tracer velocities along the lysimeter length are noticeable: while the fastest tracer movement can be seen closest to the bottom-most end (C5), a delayed response was observed at the top-most cross section (C5). **Table 1-A** summarizes this behavior, where estimated arrival times at different depths is shown for each cross-section. It can be seen that required time for the tracer to reach 0.8 m depth for cross-section C5 is almost twice as large as for C1 (10.3 days versus 6.3 days) with intermediate values happening for the cross-sections in between. Different vertical velocities might also explain the different vertical extents of the tracer plume across y-distances. There is no clear differentiation between two tracer-labelled pulses for C1, whereas a visible larger spread can be seen in C5. We believe that the differences in velocities occur mainly due to the increasing rainfall intensities from C1 towards C5, as discussed in **Section 4.1**, Additionally, the region close to C5 is constantly under wetter conditions due to its proximity to the outlet, where saturation must occur in order for water to leave through the seepage face. On the other hand, the upslope regions are relatively drier due to longer distance between the water table and the soil surface (see for example the water table in Figure 4B at t = 16h) . This length-dependent gradient of soil moisture will lead to a gradient in hydraulic conductivities which will promote the observed differences in tracer velocities. Our results are in accordance with previous modeling studies of the system under study (Pangle et al., 2017) and agree with the hydrologic functioning of natural hillslopes with impermeable bedrock (Kirkby, 1988; Graham and McDonnell, 2010). It is also possible to see a slight differential movement across the width (x-direction) for cross-sections C3 through C5, resulting in gentle slope in the observed plume. Since the skip-dipole scheme utilized should not result in any asymmetric features (as investigated in forward modelling exercises prior to the experiment – not shown here), this might indicate varying bulk densities resulting from a likely (although unintended) non-uniform packing of the soil.

Figure 7 shows the depth-average profiles of retrieved concentrations versus the estimated concentrations from the water-samplers, where a good agreement in both timing of the tracer movement as well in magnitude of the chloride concentrations can be observed. In our system, the

531 locations of the ERI cross-sections were chosen to be offset from the sampling verticals due to
532 possible interferences in the flow fields by the Prenart suction lysimeters and co-located MPS2,
533 both having their tubing and cables vertically routed to the floor of the lysimeter. In this way, we
534 do not consider the suction lysimeter interpolated onto the cross-sectional images to provide the
535 true fluid conductivity, but giving their proximity to the cross-sections and homogenous nature of
536 the soil, we believe they represent adequate approximations of fluid conductivity. An observation
537 must be made regarding cross-sections 1 and 2, which are located outside of the interpolated
538 domain provided by sampling verticals, and in the absence of an appropriate extrapolated method
539 were compared to data from the nearest sensors (vertical C1). Different approaches have been
540 used to circumvent the issue of validation of ERI-derived values of concentrations in other studies:
541 In their saturated steady state experiment, Slater et al., (2002) used conductivity sensors located
542 inside observation wells: Due to screening along the well lengths, mixing of water could occur and
543 their values of conductivity could not be considered representative of point measurements. Koestel
544 et al (2008) used TDR-based values of σ_f for validation. Although advantageous from the point of
545 reducing the interference on water flow-paths, the sensors were located on the walls of the soil
546 monolith, providing a local scale validation further from the center of the monolith. On the other
547 hand, the internal breakthrough at unsteady state conditions investigated by Wehrer and Slater
548 (2015) was only qualitatively evaluated and seepage water was used to validate their findings. We
549 further calculated the coefficient of determination (r^2) between $C_{Cl,ERT}$ and $C_{Cl,Obs}$ as a measure of
550 goodness of fit. These results are highlighted in **Table 1-B** suggesting a good performance by the
551 ERI estimates of chloride concentration, with overall high values of goodness of fit. It is possible
552 to observe that C1 and C2 obtained the lowest r^2 values, which might be related to the use of the
553 nearest sampled values of conductivity of background conductivity. The diffuse character of
554 electric fields (e.g. Kemna et al., 2002) and the smoothness imposed by the regularization scheme
555 used in the inversion procedure play an important role when assessing ERI versus in-situ
556 observations: It is important to note that comparing point specific values of concentration as shown
557 in **Figure 7** to sampled results are more useful when promoting a qualitative analysis than a precise
558 comparison between observation and predicted quantities.

559

560

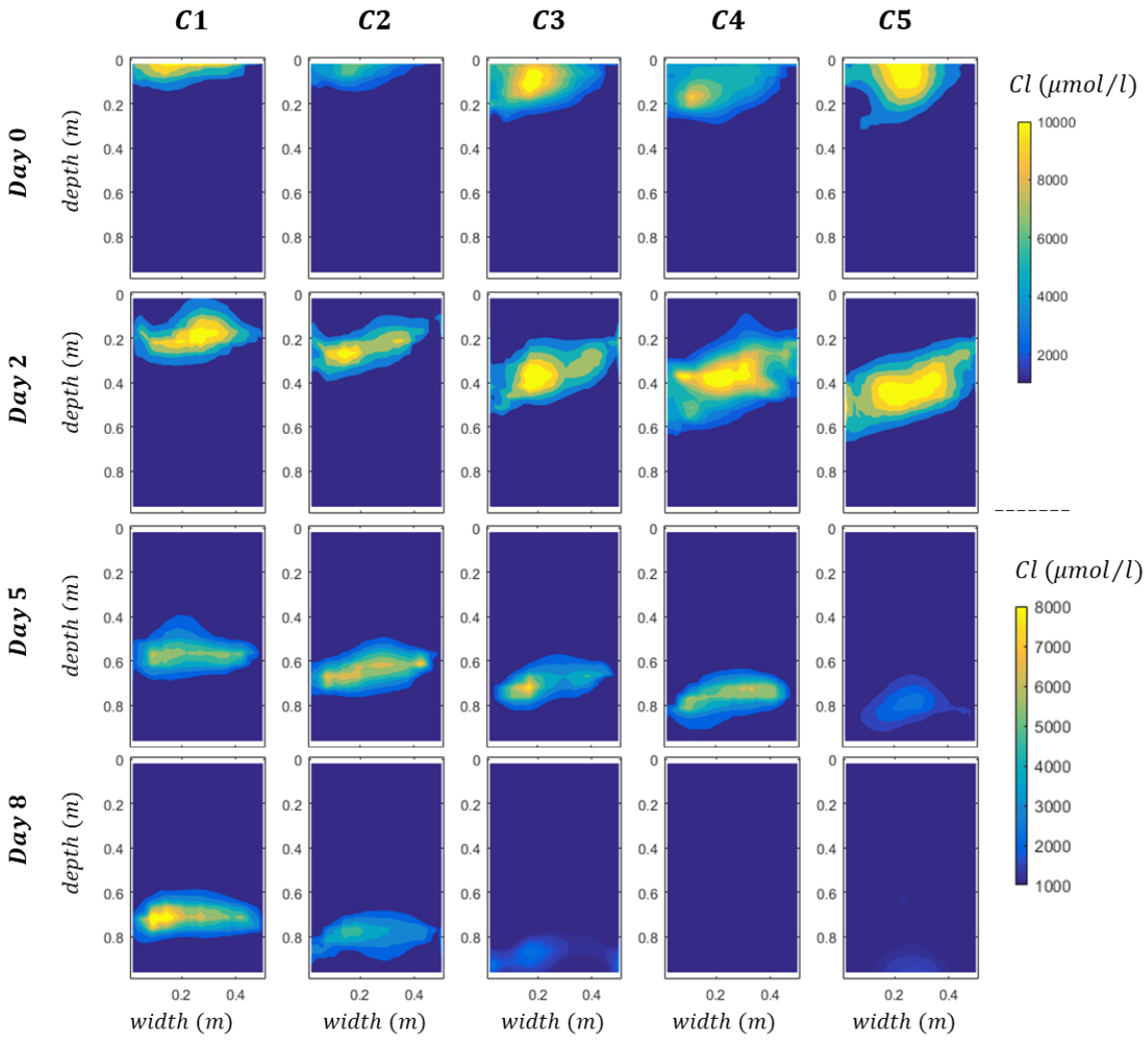

Figure 6. Retrieved images of Chloride concentration per cross-section for different days with respect to the injection day (day 0) taken at a reference time (14:00). Note that the scale of the color bar is different between images from July 6th and 8th (early response) and July 11th and 14th (late response).

571

572

573 **Table 1. A- Estimated tracer arrival times at different depths. B- Goodness of fit between $C_{Cl,ERT}$ and $C_{Cl,Obs}$**

A

	Arrival time (days)				
Depth (cm)	***C.1***	***C.2***	***C.3***	***C.4***	***C.5***
10	0.5	2.1	0.4	0.2	0.4
25	2.4	2.4	2.2	2.2	2.2
50	4.7	4.4	3.3	2.6	2.4
80	10.3	8.3	6.4	6.3	6.3

B

	Goodness of fit (R^2)				
	C.1	***C.2***	***C.3***	***C.4***	***C.5***
R^2	0.79	0.80	0.87	0.89	0.95

574

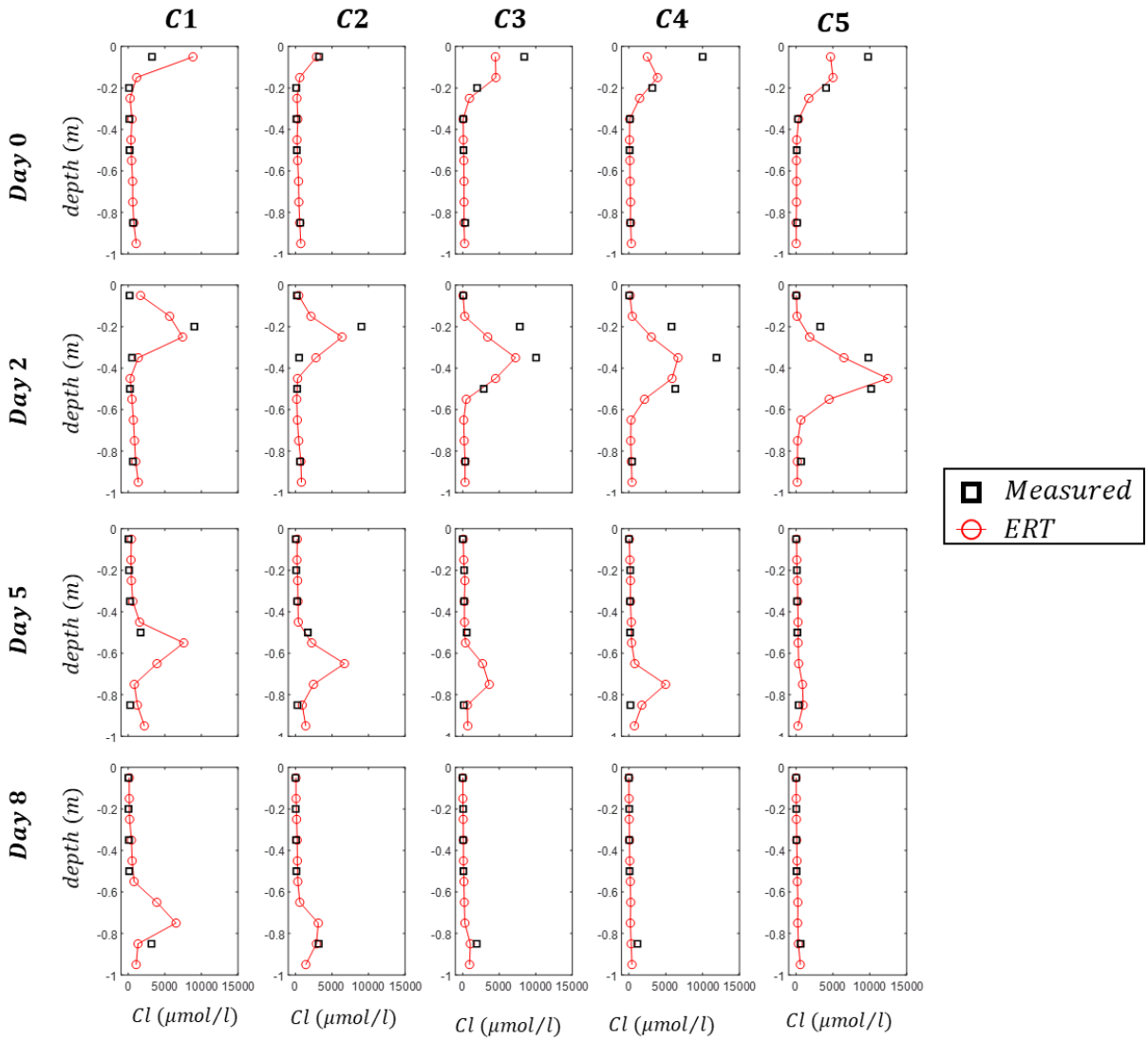

Figure 7. Depth-averaged ERI-derived concentrations versus measured concentrations at cross-sections C1 trough C5 at the same days as in Figure 5. Measured concentrations for each profile were obtained through interpolation of values at the sampling verticals.

4.4. Lysimeter-scale solute breakthrough

Here, we attempt to reconcile the 2D images of spatially interpolated chloride concentration described in **Section 3.4.3** with the knowledge on the water table fluctuations to further investigate the lysimeter-scale chloride breakthrough, and explain the delayed response in discharge conductivity after the first recovery-period irrigation cycle (cycle 9, day 2), as seen in **Figure 3-C**.

Figure 8 provides an overlook of both ERI-derived solute movement and water table position at different times for the injection cycle (day 0) and first recovery cycle (day 2). The time stamps shown here were chosen to best represent the temporal dynamic described previously (see **Figure 4**), in which t = 3h represents the first peak in water table at the end of the first irrigation pulse, t = 5h represents an intermediate water table height following a quick 2-hour recession prior to the second pulse, whereas t = 8h represents the water table at its highest level, immediately after the second irrigation pulse. Additionally, **Figure 8G** shows the progression of the Chloride concentrations measured at the seepage face, with the timesteps of snapshots shown as vertical bars.

It can be seen that the tracer occupied a well-defined region within the first 25 cm of soil after the second irrigation pulse in day 0 (**Figure 8C).** It is possible to see that no tracer response has been detected at the seepage face for that day whereas the highest water table levels reached for that day were located sufficiently far from the tracer-dominated region. On the other hand, on day 2 the tracer plume is pushed down further by the imposed irrigation pulses, allowing for a higher proximity between tracer dominated region and water table, which ultimately lead to the mobilization of the tracer. According to **Figure 8F**, most of the injected solute was placed above the water table at Day2, 8 hr. However, the solute concentration of discharge at that time is already high, which suggests the occurrence of lateral (along the y-direction) flow above the water table in the tension-saturated zone as the main process responsible for the quick tracer mobilization. The absence of an ERI cross-section closest to the seepage makes it impossible to accurately describe the chloride concentrations around that area, but the overall shape of the tracer plume suggests an even deeper depths were reached within that region. It is also important to observe the differences between water table heights between both days, in which malfunctioning of the irrigation system being most likely the cause for the lower values of irrigation for day 0, resulting in lower water table levels. An animation containing the variables in Figures 3 and 8 showing the progression of the experiment is provided as a supplement (See Supplements Section) to aid the interpretation of the results.

Additional insights on the ability the proposed method to properly reproduce the chloride breakthrough within the lysimeter are presented in **Figure 9**, where the observed Chloride mass (μmol) inside the lysimeter (red line) is compared to the ERI-based one (black dashed line).

Highlighted as gray bars are the irrigation pulses applied throughout the period. The tracer injection, marked by the initial jump in M_{Cl} at day 0 is followed by a period with constant values between days 0 and 2, while the extent of solute removal from the lysimeter observed as sequential drops in M_{Cl} due to the applied irrigation pulses (gray bars). An overall good agreement can be seen, in which the ERI derived Chloride mass closely follows the mass-balance values, with the exception of the time period between days 1 and 2, in which the ERI based estimates show a visible increase in mass, even though the system does not experience any irrigation pulse during that time. Differences in mass within the system can also be seen for the two last irrigation cycles, marked by an overprediction of M_{Cl} from ERI derived.

4.5. Towards a local understanding of hillslope-scale processes

The observation that hillslopes and catchments in general possess much faster runoff responses to rainfall events when compared to the delayed transit time responses has been subject to recent attention (Botter et al., 2010; Hrachowitz et al., 2013; McDonnel and Beven, 2014), and the differentiation between hydrologic responses in terms of celerity (i.e. hydraulic response) and velocity (i.e. velocity of water molecules) has been proposed as a path forward for the development of more physically sound watershed models. Verseveld et al., (2017) conducted a field-scale sprinkling experiment in a natural hillslope at the H. J. Andrews Experimental Forest in western Oregon and investigated the interplay between the slower, unsaturated (vertical), versus faster, saturated (lateral) flow paths, mediated by soil depths, in explaining the differences in celerity-velocity responses. Scaini et al., (2018) performed a hillslope-scale sprinkling experiment at the Weierbach catchment in Luxembourg and observed that bedrock topography to be an important controlling factor on the orientation of subsurface flow pathways. Quick tracer mobilization across the tension saturated zone for the same soil lysimeter as in our study was also suggested by a modelling exercise in which a more intense and less spaced irrigation scheme was imposed to the lysimeter leading to higher water tables (Pangle et al., 2017) .

While our study lacks the representation of field-scale heterogeneities such as in variable soil depths (Verseveld et al., 2018) and complex bedrock topography (Scaini et al., 2018), our choice for simple and controllable system allowed the observation of smaller scale processes that can be upscaled for leveraging hillslope scale understanding. The sequential solute release as discharge associated with periods with the occurrence of an active saturated zone highlight the dynamic role

of water table fluctuations as a mediator between the occurrence of slower vertical versus faster lateral flow paths. It is worth noting that while the uniform soil depth and intense irrigation sequence imposed in our experiment might not be realistic for most natural hillslopes, the processes presented here can be associated with those of humid catchments, or seasonally occurring water tables. Additionally, while soil depth might play a more important role at controlling the occurrence of slower and faster flow paths at the hillslope scale (Verseveld et al., 2017), we believe that our experiment can also be representative of near stream shallow water table dynamics.

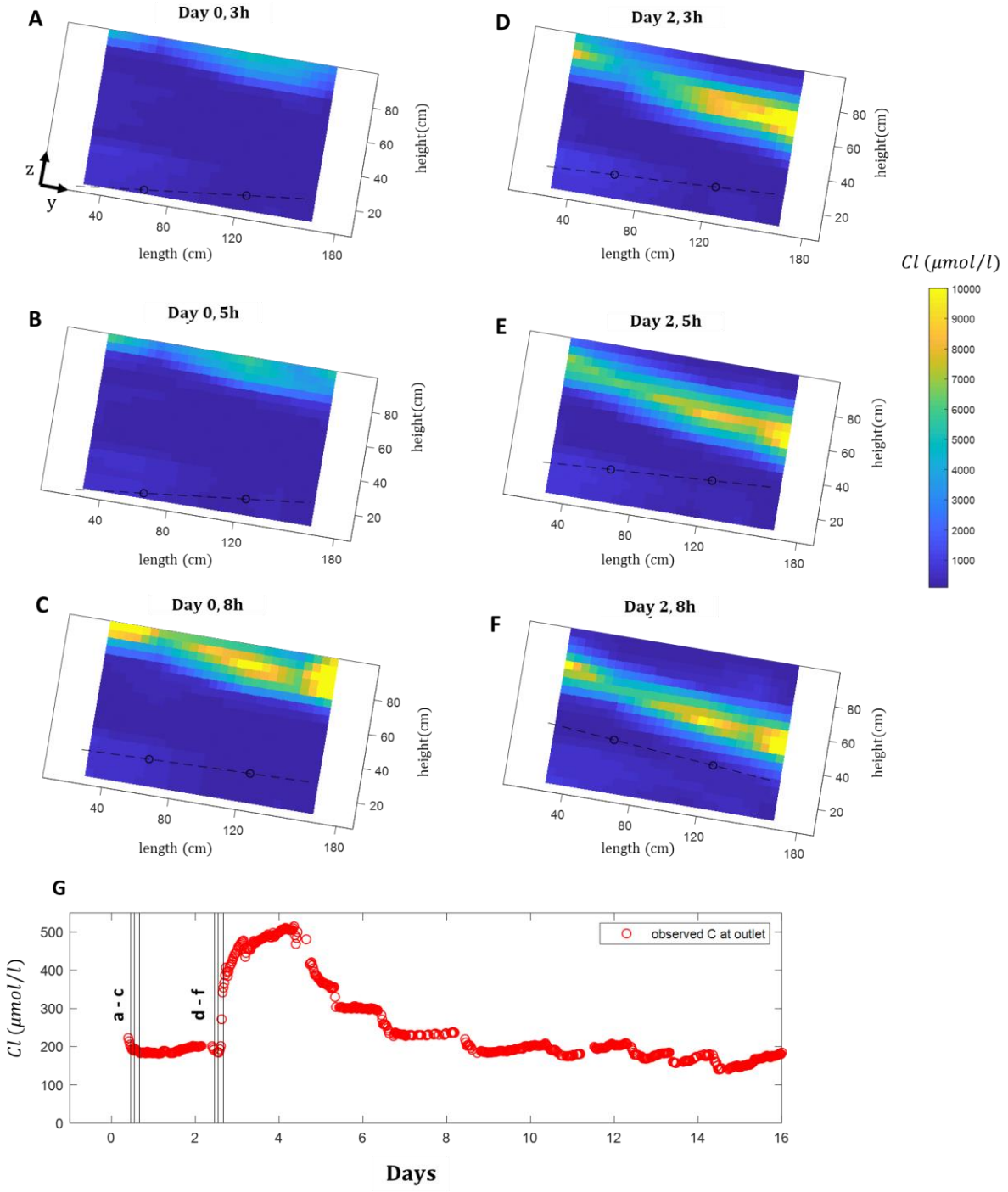

654

Figure 8. (a-f) Interpolated ERT-derived panels showing Chloride concentration in μmol/l throughout days 0 and 2 (tracer injection and following irrigation cycle). Dashed black lines indicate the approximate location of the water table, estimated by pressure transducer measurements at 2 points (circles). g. Estimated Chloride concentration from discharge samples, highlighting the time-steps for which the panels a-f were taken.

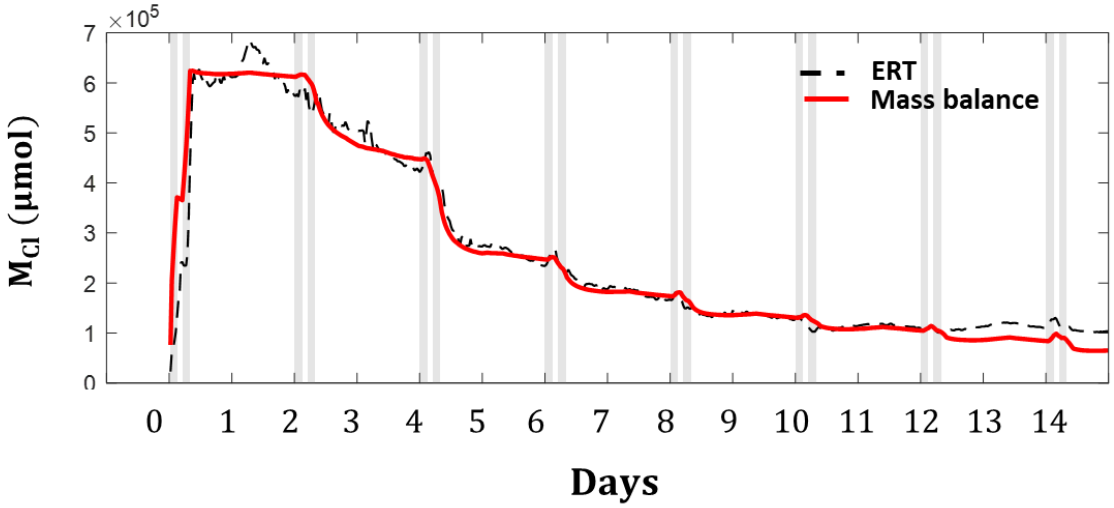

Figure 9. Chloride mass inside the lysimeter starting from the injection day (day 0) and following the recovery cycles (day 2 onwards). The red line represents the Chloride mass estimated through the mass balance (M_{obs}, Eq. 19), whereas the dashed black line represents the ERI-derived values (M_{ERT}). Irrigation pulses are shown as grey bars.

5. SUMMARY AND CONCLUSION

Adequate quantification of residence times of water in natural landscapes can reveal important mechanisms of CZ functioning. Existing theories on transit time's distribution are commonly applied as lumped representations of hydrologic systems and lack confirmation from experiments that explicitly address the internal variability of flow and transport processes.

ERI represents a consolidated tool for the tracking of tracers at the subsurface and has the potential to provide insight into residence times of water of natural systems. While the natural variability of biogeochemical processes at the CZ is highly correlated to landscape morphology which is commonly studied at the hillslope scale, laboratory experiments using ERI have so far focused on soil lysimeters or monoliths where vertical fluxes of water prevail. While the adequate representation of hillslope processes involves the consideration of variable moisture states and fluxes, such conditions have traditionally posed challenges for studies of tracer movement using ERI.

This study introduced the use of ERI as a tool for the investigation of the processes leading to the varying residence times of water on a sloping soil lysimeter representing hydrologic processes common in natural hillslopes. We present a simple method for quantification of tracer movement at the subsurface under transient conditions and varying moisture states over space and time. We demonstrated that the PSS theory (Harman and Kim, 2014) can be applied to the equations governing the electrical conductivity of soils to provide a simple solution to the tracer movement under complex conditions, and introduced the experimental procedures to be carried for different soils, with respect to the existence of surface conductivity. Our method is advantageous over the existing approaches in that it does not require knowledge of petrophysical properties of the material for estimating fluid conductivities that can be applied at transient conditions.

We imposed a regimented irrigation scheme at soil in the form of irrigation cycles, in which the internal states and fluxes would repeat themselves. We then added a conductive tracer to one of the cycles and retrieved values of fluid conductivity through a simple conversion based

on the response recorded during the cycles prior to injection. This led us to quantitatively observe the internal tracer breakthrough and quantify the time necessary for the tracer to travel vertically through different regions of the lysimeter. We observed the differential movement of solutes in which shorter transit times were observed at regions closer to the outlet as opposed to the slower movement of the tracer at the upslope region. The observed difference was almost twofold, which considering the dimensions of our system can highlight the heterogeneity in hydrologic transport observed at the hillslope scale.

Even though an exact estimate of observed fluid conductivity was not possible due to the location of water samples, our results show that the method could satisfactorily provide estimates of fluid conductivity and therefore tracer concentrations within the soil lysimeter. We suggest that similar studies using full 3D ERI surveys can provide better assessment between observed values and ERI estimates and provide a complete investigation throughout the intended control volume.

Finally, we were able to explore the lysimeter-scale solute export at transient conditions, by combining the spatially distributed images of the tracer progression throughout the lysimeters length with the associated water table fluctuations. Our results highlight the role of water table fluctuations as a mechanism for the quick tracer mobilization and suggest the occurrence of such process for humid or seasonally humid regions, as well as near stream portions of hillslopes.

ACKNOWLEDGEMENTS

Antonio A. M. N. would like to acknowledge the financial support received by the Brazilian Ministry of Education through the CAPES Foundation and the State of Espírito Santo through the FAPES foundation. We would like to thank Ty Ferré (University of Arizona) and Andrew Binley (Lancaster University) on suggestions on electrode design and Michael Tso (Lancaster University) for the support with the program R3. Additionally, the authors would like to thank the Biosphere 2 staff involved in the operational aspects of the experiment: Aaron Bugaj, Nate Abramson, Wei-Ren Ng and Edward Hunt. Upon acceptance, the data used in this study will be available through: https://figshare.com/authors/Antonio_Meira/8292240

REFERENCES

Alumbaugh, D. L., Labrecque, D., Technologies, M., Yeh, T. C. J., De-fg-, G. N., Project, G., & Roland, O. (n.d.). US Department of Energy A HYDROLOGIC - GEOPHYSICAL METHOD FOR CHARACTERIZING FLOW AND TRANSPORT PROCESSES WITHIN THE VADOSE ZONE Project Number : 70267.

Bellmunt, F., Marcuello, A., Ledo, J., & Queralt, P. (2016). Capability of cross-hole electrical configurations for monitoring rapid plume migration experiments. *Journal of Applied Geophysics*, *124*, 73–82. https://doi.org/10.1016/j.jappgeo.2015.11.010

Binley, A., Henry-Poulter, S., & Shaw, B. (1996). Examination of solute transport in an undisturbed soil column using electrical resistance tomography, *32*(4), 763–769.

Binley, A. (2013), R3t, Version 1.8., Lancaster Univ., Lancaster, U. K. (Available at http://www.es.lancs.ac.uk/people/amb/Freeware/Freeware.htm.)

Binley, A., Hubbard, S. S., Huisman, J. A., Revil, A., Robinson, D. A., Singha, K., & Slater, L. D. (2015). The emergence of hydrogeophysics for improved understanding of subsurface

processes over multiple scales. *Water Resources Research*, *51*, 3837–3866. https://doi.org/10.1002/2015WR017016.

Botter, G., Bertuzzo, E., and Rinaldo, A. (2010), Transport in the hydrologic response: Travel time distributions, soil moisture dynamics, and the old water paradox, Water Resour. Res., 46, W03514, doi:10.1029/2009WR008371.

Brantley, S. L., Goldhaber, M. B., & Vala Ragnarsdottir, K. (2007). Crossing disciplines and scales to understand the critical zone. *Elements*, *3*(5), 307–314. https://doi.org/10.2113/gselements.3.5.307

Brooks, P. D., Chorover, J., Fan, Y., Godsey, S. E., Maxwell, R. M., McNamara, J. P., & Tague, C. (2015). Hydrological partitioning in the Critical zone: Recent advances and opportunities for developing transferable understanding of water cycle dynamics. *Water Resources Research*, 1–15. https://doi.org/10.1002/2015WR017039.Received

Campbell, R. B., Bower, C. A., & Richards, L. A. (1948). Change of Electrical Conductivity With Temperature and the Relation of Osmotic Pressure to Electrical Conductivity and Ion Concentration for Soil Extracts. Soil Science Society of America Journal, 13(C), 66–69. https://doi.org/10.2136/sssaj1949.036159950013000c0010x

Chorover, J., Kretzschmar, R., Garica-Pichel, F., & Sparks, D. L. (2007). Soil biogeochemicial processes within the critical zone. *Elements*, *3*(5), 321–326. https://doi.org/10.2113/gselements.3.5.321

Dontsova, K., Steefel, C. I., Desilets, S., Thompson, a., & Chorover, J. (2009). Coupled modeling of hydrologic and geochemical fluxes for prediction of solid phase evolution in the Biosphere 2 hillslope experiment. *Hydrology and Earth System Sciences Discussions*, *6*, 4449–4483. https://doi.org/10.5194/hessd-6-4449-2009

Friedman, S. P. (2005). Soil properties influencing apparent electrical conductivity: A review. *Computers and Electronics in Agriculture*, *46*(1–3 SPEC. ISS.), 45–70. https://doi.org/10.1016/j.compag.2004.11.001

769 Geuzaine, C., & Remacle, J.-F. (2009). Gmsh: A 3-D finite element mesh generator with built-in
770 pre- and post-processing facilities. *International Journal for Numerical Methods in*
771 *Engineering*, *79*(11), 1309–1331. https://doi.org/10.1002/nme.2579

772 Graham, C. B., & McDonnell, J. J. (2010). Hillslope threshold response to rainfall: (2)
773 Development and use of a macroscale model. *Journal of Hydrology*, *393*(1–2), 77–93.
774 https://doi.org/10.1016/j.jhydrol.2010.03.008

775 Grunat, D. A., Slater, L. D., & Wehrer, M. (2013). Complex Electrical Measurements on an
776 Undisturbed Soil Core: Evidence for Improved Estimation of Saturation Degree from
777 Imaginary Conductivity. *Vadose Zone Journal*, *12*(4), 0.
778 https://doi.org/10.2136/vzj2013.03.0059

779 Harman, C. J., & Kim, M. (2014). An efficient tracer test for time-variable transit time
780 distributions in periodic hydrodynamic systems. *Geophysical Research Letters*, *41*(5),
781 1567–1575. https://doi.org/10.1002/2013GL058980

782 Heimsath, A. M., & Burke, B. C. (2013). The impact of local geochemical variability on
783 quantifying hillslope soil production and chemical weathering. *Geomorphology*, *200*, 75–
784 88. https://doi.org/10.1016/j.geomorph.2013.03.007

785 Hrachowitz, M., Savenije, H., Bogaard, T. A., Tetzlaff, D., and Soulsby, C. (2013). What can
786 flux tracking teach us about water age distribution patterns and their temporal dynamics?,
787 Hydrol. Earth Syst. Sci., 17, 533–564, https://doi.org/10.5194/hess-17-533-2013,

788 Kemna, A., Kulessa, B., & Vereecken, H. (2002). Imaging and characterisation of subsurface
789 solute transport using electrical resistivity tomography (ERT) and equivalent transport
790 models. *Journal of Hydrology*, *267*(3–4), 125–146. https://doi.org/10.1016/S0022-
791 1694(02)00145-2

792 Kim, M., Pangle, L. A., Cardoso, C., Lora, M., Volkmann, T. H. M., Wang, Y., … Troch, P. A.
793 (2016). Transit time distributions and StorAge Selection functions in a sloping soil
794 lysimeter with time-varying flow paths: Direct observation of internal and external transport

795 variability. *Water Resources Research*, *52*, 7105–7129.
796 https://doi.org/10.1002/2016WR018620.Received

797 Kirkby, M. (1988). Hillslope runoff processes and models. *Journal of Hydrology*, *100*(1–3),
798 315–339. https://doi.org/10.1016/0022-1694(88)90190-4

799 Koestel, J. K., Moeys, J., & Jarvis, N. J. (2011). Evaluation of Nonparametric Shape Measures
800 for Solute Breakthrough Curves. *Vadose Zone Journal*, *10*(4), 1261.
801 https://doi.org/10.2136/vzj2011.0010

802 Koestel, J., Kemna, A., Javaux, M., Binley, A., & Vereecken, H. (2008). Quantitative imaging of
803 solute transport in an unsaturated and undisturbed soil monolith with 3-D ERT and TDR.
804 *Water Resources Research*, *44*(12), 1–17. https://doi.org/10.1029/2007WR006755

805 LaBrecque, D. J., and X. Yang (2001), Difference inversion of ERT data: A fast inversion
806 method for 3-D in situ monitoring, J. Environ. Eng. Geophys., 6, 83-89.
807 https://doi.org/10.4133/JEEG6.2.83

808 Looms, M. C., Jensen, K. H., Binley, A., & Nielsen, L. (2008). Monitoring Unsaturated Flow
809 and Transport Using Cross-Borehole Geophysical Methods. *Vadose Zone Journal*, *7*(1),
810 227. https://doi.org/10.2136/vzj2006.0129

811 Lybrand, R. A., & Rasmussen, C. (2014). Linking soil element-mass-transfer to microscale
812 mineral weathering across a semiarid environmental gradient. *Chemical Geology*, *381*, 26–
813 39. https://doi.org/10.1016/j.chemgeo.2014.04.022

814 Lybrand, R. A., & Rasmussen, C. (2018). Climate, topography, and dust influences on the
815 mineral and geochemical evolution of granitic soils in southern Arizona. *Geoderma*,
816 *314*(December 2017), 245–261. https://doi.org/10.1016/j.geoderma.2017.10.042

817 Maher, K. (2011). The role of fluid residence time and topographic scales in determining
818 chemical fluxes from landscapes. *Earth and Planetary Science Letters*, *312*(1–2), 48–58.
819 https://doi.org/10.1016/j.epsl.2011.09.040

Maher, K. (2010). The dependence of chemical weathering rates on fluid residence time. *Earth and Planetary Science Letters*, *294*(1–2), 101–110. https://doi.org/10.1016/j.epsl.2010.03.010

McDonnell, J. J., and Beven, K. (2014), Debates—The future of hydrological sciences: A (common) path forward? A call to action aimed at understanding velocities, celerities, and residence time distributions of the headwater hydrograph, Water Resour. Res., 50, 5342–5350, doi:10.1002/2013WR015141.

McGuire, K. J., & McDonnell, J. J. (2006). A review and evaluation of catchment transit time modeling. *Journal of Hydrology*, *330*, 543–563. https://doi.org/10.1016/j.jhydrol.2006.04.020

Mike, K. (1988). Hillslope runoff processes and models. *Journal of Hydrology*, *100*(1–3), 315–339. Retrieved from http://www.sciencedirect.com/science/article/pii/0022169488901904

Perri, M. T., Cassiani, G., Gervasio, I., Deiana, R., & Binley, A. (2012). A saline tracer test monitored via both surface and cross-borehole electrical resistivity tomography: Comparison of time-lapse results. *Journal of Applied Geophysics*, *79*, 6–16. https://doi.org/10.1016/j.jappgeo.2011.12.011

Pohlmann, M., Dontsova, K., Root, R., Ruiz, J., Troch, P., & Chorover, J. (2016). Pore water chemistry reveals gradients in mineral transformation across a model basaltic hillslope. *Geochemistry, Geophysics, Geosystems*, *17*(6), 2054–2069. https://doi.org/10.1002/2016GC006270

Rhoades, J. D. (1981). Predicting Bulk Soil Electrical Conductivity versus Saturation Paste Extract Electrical Conductivity Calibrations from Soil Properties. *Soil Sci Soc Am J*, *45*(1), 42–44. Retrieved from http://soil.scijournals.org/cgi/content/abstract/soilsci;45/1/42

Samouëlian, a., Cousin, I., Tabbagh, a., Bruand, a., & Richard, G. (2005). Electrical resistivity survey in soil science: A review. *Soil and Tillage Research*, *83*, 173–193. https://doi.org/10.1016/j.still.2004.10.004

Scaini, A., Hissler, C., Fenicia, F., Juilleret, J., Iffly, J. F., Pfister, L., & Beven, K. (2018). Hillslope response to sprinkling and natural rainfall using velocity and celerity estimates in a slate-bedrock catchment. Journal of Hydrology, 558, 366–379. https://doi.org/10.1016/j.jhydrol.2017.12.011

Singha, K., & Gorelick, S. M. (2006). Hydrogeophysical tracking of three-dimensional tracer migration: The concept and application of apparent petrophysical relations. *Water Resources Research*, *42*(6), 1–14. https://doi.org/10.1029/2005WR004568

Slater, L., Binley, a., Versteeg, R., Cassiani, G., Birken, R., & Sandberg, S. (2002). A 3D ERT study of solute transport in a large experimental tank. *Journal of Applied Geophysics*, *49*, 211–229. https://doi.org/10.1016/S0926-9851(02)00124-6

Slater, L., Binley, A. M., Daily, W., & Johnson, R. (2000). Cross-hole electrical imaging of a controlled saline tracer injection. *Journal of Applied Geophysics*, *44*(2–3), 85–102.

Slater, L., Binley, A. ., Daily, W., & Johnson, R. (2000). Cross-hole electrical imaging of a controlled saline tracer injection. *Journal of Applied Geophysics*, *44*(2–3), 85–102. https://doi.org/10.1016/S0926-9851(00)00002-1

van Verseveld, W. J., Barnard, H. R., Graham, C. B., McDonnell, J. J., Brooks, J. R., and Weiler, M.: A sprinkling experiment to quantify celerity–velocity differences at the hillslope scale, Hydrol. Earth Syst. Sci., 21, 5891–5910, https://doi.org/10.5194/hess-21-5891-2017, 2017.

Vázquez-Ortega, A., Huckle, D., Perdrial, J., Amistadi, M. K., Durcik, M., Rasmussen, C., … Chorover, J. (2016). Solid-phase redistribution of rare earth elements in hillslope pedons subjected to different hydrologic fluxes. *Chemical Geology*, *426*, 1–18. https://doi.org/10.1016/j.chemgeo.2016.01.001

Wang, C., McNew, C. P., Lyon, S. W., Walter, M. T., Volkman, T. H. M., Abramson, N., … Dahlke, H. E. (2019). Particle tracer transport in a sloping soil lysimeter under periodic, steady state conditions. *Journal of Hydrology*, *569*(December 2018), 61–76. https://doi.org/10.1016/j.jhydrol.2018.11.050

Wherer, M., & Slater, L. D. (2014). Characterization of water content dynamics and tracer breakthrough by 3-D electrical resistivity tomography (ERT) under tranient unsaturated conditions. *Water Resources Research*, *50*(7), 5510–5531. https://doi.org/10.1002/2013WR014910.Received

Zapata-Rios, X., Brooks, P. D., Troch, P. A., McIntosh, J., & Guo, Q. (2016). Influence of terrain aspect on water partitioning, vegetation structure and vegetation greening in high-elevation catchments in northern New Mexico. *Ecohydrology*, *9*(5), 782–795. https://doi.org/10.1002/eco.1674